Engineering Geology 297 (2022) 106485

Contents lists available at ScienceDirect

Engineering Geology

journal homepage: www.elsevier.com/locate/enggeo

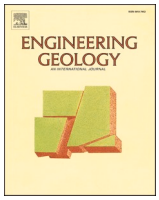

Site-scale liquefaction potential analysis using a sectional random field model

Amir Gholampour *

Department of Civil Engineering, Apadana Institute of Higher Education, Shiraz, Iran

ARTICLE INFO

Keywords:
Liquefaction potential
Conditional random field
Site-scale analysis
Cone penetration test

ABSTRACT

This paper presents a new random field modeling to assess the site-scale spatial variability of soil properties applied in liquefaction mapping. In this procedure, the initial random fields are primarily generated, based on in-situ measured data. These initial fields are considered as the virtual known values to construct interior random fields, section-by-section and around a central axis. Assembling these sections results in a three-dimensional random field model. Through this approach, more accurate vertical semivariogram models can be available, in addition to a higher number of measured data involved in the generation of random fields. Based on a verification procedure, computational cost reduction and a more appropriate prediction of the layering characteristics are the two most important beneficial points of changing the modeling strategy from planar to sectional. The proposed approach is implemented in a case study in Oceano, California and the spatial distribution of liquefaction probability is estimated. It is concluded that the sectional random field can efficiently locate the liquefiable zone through the soil volume, based on liquefaction evidence. In addition to performing the liquefaction severity assessment, it is also illustrated that the hazard assessments based on liquefaction severity alone cannot provide the comprehensive prediction of liquefaction potential and may lead to unconservative engineering judgments.

1. Introduction

One of the most destructive causes of ground failure during earthquakes is the liquefaction phenomenon, which results in a sudden loss of strength and stiffness in saturated loose sandy deposits. A wide range of damages has been reported regarding the matter of regional and site-scale liquefaction (Youd and Idriss, 2001; Lee et al., 2004; Caputo and Papathanassiou, 2012; Lin et al., 2021).

Several attempts have been made to predict liquefaction potential over the last decades, using empirical correlations. These correlations have been commonly developed based on soil properties measured by in-situ tests such as the Cone Penetration Test (CPT) (Robertson and Wride, 1998; Geyin and Maurer, 2021), standard penetration test (Tunusluoglu and Karaca, 2018), and the shear wave velocity test (Zhang et al., 2021).

Due to exploration cost, the soil properties utilized in assessing liquefaction potential (e.g., the tip resistance and the side friction from CPT measurements) can only be measured in a limited portion of the total soil volume, where the test is performed. Hence, the corresponding values remain unknown at the other soil spots that are apart from the test locations. This fact indicates that there are indeed uncertainties involved in soil liquefaction identification, and the problem must be treated in the probabilistic framework (Juang et al., 1999).

The nature of uncertainty is generally related to the inherent spatial variability of soil properties. Probabilistic studies have demonstrated that ignoring spatial variability may lead to an unconservative estimation of soil liquefaction (Na et al., 2009; Vivek and Raychowdhury, 2014). In an effort to address the soil spatial variability, the random field theory has been developed for geostatistical practice. Numerous researches have focused on applying two-dimensional (2D) and three-dimensional (3D) random field-based approaches in liquefaction potential evaluation in recent decades (Dawson and Baise, 2005; Popescu et al., 2005; Lenz and Baise, 2007; Bong and Stuedlein, 2018; Shen et al., 2019; Zhao et al., 2021).

For instance, Wang and Chen (2018) have exploited the CPT records to obtain the index of liquefaction potential at soundings locations. Afterward, these data have been applied as inputs to 2D surficial multi-scale random field modeling. This procedure, (i.e., *the averaged index*

* Corresponding author.
E-mail address: a.gholampour1988@gmail.com.

https://doi.org/10.1016/j.enggeo.2021.106485
Received 12 February 2021; Received in revised form 1 August 2021; Accepted 30 November 2021
Available online 8 December 2021

approach) is simple and computationally efficient. However, the complex subsurface heterogeneity associated with soil properties' spatial variability has not been addressed in this approach.

Greenfield and Grant (2020) have applied Gaussian process models into liquefaction evaluating procedures in a more comprehensive analysis. In this regard, 3D estimates of the liquefaction probability have been produced for a case study. Although the 3D random field simulation of soil properties provides a full-scale correlation analysis, it significantly increases the computational cost. Additionally, it may not always guarantee a more accurate result in liquefaction mapping (Wang et al., 2017b). The full 3D random fields can be time-consuming and usually challenging to carry out technically.

Therefore, several researchers have preferred to utilize the extended 2D random field, termed the *Local Soil Property* (LSP) approach, for modeling the spatially correlated soil properties (Baker and Faber, 2008; Wang et al., 2017b; Juang et al., 2018). In this approach, random fields are generated in a layer-by-layer sequence, and the planar correlation structure is assessed at each level for soil properties. Assembling planar random fields results in a volumetric simulation model (Wang et al., 2017b). In the regional-scale analysis (i.e., over hundreds of square kilometers), where usually sampled data are abundantly available, this approach provides an acceptable surficial liquefaction potential characterization (Uzielli et al., 2005; Liu and Chen, 2006).

On the other hand, in the site-scale analysis (e.g., infrastructures such as buildings, bridge foundations, and soil slopes), fewer explorations are usually carried out, and insufficient information is available about the soil's heterogeneous structure. The measured data is usually obtained in one direction that is perpendicular to the ground surface. The absence of sufficient known data may increase the planar simulation variance; accordingly, it may decrease the random fields' efficiency. Furthermore, the spatial correlation of soil properties in the planar method (i.e., LSP approach) is merely modeled in the horizontal direction (i.e., perpendicular to the sedimentation direction), which represents a significantly higher scale of variation versus the vertical direction. Thus, an efficient method is necessitated that can be applied for site-scale liquefaction prediction and to resolve the reviewed available deficiencies.

The primary scope of the present paper is to introduce a procedure for constructing a 3D random field in a section-by-section sequence for CPT parameters. Through this approach, more accurate vertical semivariogram models will be available, in addition to a higher number of measured data involved in the generation of random fields, thanks to the relatively high sampling frequency of the CPTs in the vertical direction. This type of modeling can be advantageous for the examination of the site-scale soil liquefaction problems that are always accompanied by limitations of data measurement. Another objective of this research is to identify the liquefiable zone throughout the model volume, based on the spatial distribution of Probability of Liquefaction (PL). Furthermore, it has been aimed to implement the proposed procedure in a site-scale liquefaction potential characterization for a case study.

For realizing such purposes, a computer program is designed in MATLAB to conduct the required numerical calculations. In the proposed framework, at first, the initial section's random fields are generated, based on measured CPT data. To exploit the most number of CPT soundings at each initial random field, a central CPT is selected, which is shared in all sections. Subsequently, initial sections that are considered the virtual known data are utilized to construct interior random fields, pivoted around the central CPT axis. Assembling these random field sections results in a cylindrical shape model for soil properties. After describing the steps in the proposed approach, the basis of the model is verified and the advantages are proved. The proposed procedure is implemented for a case study in Oceano, California. Based on simulations of 3D random fields for CPT parameters, the spatial distribution of the PL is predicted and applied in the liquefaction severity assessment. Finally, the results are compared with conventional liquefaction potential indicators.

2. Evaluation of liquefaction potential

In this paper, the correlation-based "simplified procedure" (Seed and Idriss, 1971; Youd and Idriss, 2001) is utilized to investigate the liquefaction occurrence. This procedure is straightforward and provides a process for avoiding undisturbed sampling. Typically, the factor of safety against liquefaction (*FS*) at any specific location is calculated by:

$$FS = CRR/CSR \tag{1}$$

where *CRR* and *CSR* respectively represent, the cyclic resistance and cyclic stress ratio. Details of *CSR* and *CRR* calculation are summarized in Appendix A or can be found in the study of Juang et al. (2003). In the present paper, the measured tip resistance (q_c) and the side friction (f) are considered spatially cross-correlated variables in the probabilistic analysis.

Another influential soil parameter in the stochastic analysis of liquefaction is the unit weight which is applied to calculate overburden stresses. In this regard, an attempt is made to use merely CPT data without any borehole sampling. Hence, the total unit weight of soil (γ) is approximated according to the CPT-based correlation equation, proposed by Robertson and Cabal (2010) as follows:

$$\gamma/\gamma_w = 0.27[log(f/q_c)] + 0.36[log(q_c/p_a)] + 1.236 \tag{2}$$

where γ_w represents the unit weight of water and p_a indicates the atmospheric pressure. Through this approach, the spatial variability of unit weight is also included in the prediction of liquefaction occurrence.

The severity of liquefaction destruction can be quantified for an entire CPT sounding using the well-known Liquefaction Potential Index (LPI), based on the original study by Iwasaki (1978). This index property which is considered an estimate of liquefaction-related surface damage can be calculated in a discretized form as follows:

$$LPI = \sum_{i=1}^{N} \omega_i F_{Li} H_i \tag{3}$$

where N and H_i are the number and the thickness of soil layers, respectively. Moreover, F_L is defined using the following equation:

$$F_L = \begin{cases} 0 & FS \geq 1.2 \\ 1 - FS & FS \leq 0.95 \\ 2 \times 10^6 e^{-18.42FS} & 0.95 \leq FS \leq 1.2 \end{cases} \tag{4}$$

In this study, only the first 10 m depth of CPT data is considered, hence the modified depth weighting factor is used as follows (Özocak and Sert, 2010):

$$\omega = 20 - 2z \tag{5}$$

In the probabilistic analysis, the F_L in Eq. (3) can be replaced with the PL and the LPI is re-named as Liquefaction Severity Index (LSI). The liquefaction indices (i.e., LPI and LSI) are widely applied for prediction of the surficial liquefaction manifestations; however, interpreting the results must be regarded with particular concerns (Van Ballegooy et al., 2015). Consequently, calibration in order to determine the liquefaction severity has been mostly attended by related researchers (Chung and David Rogers, 2017; Kim et al., 2020). It must be noticed that a more diverse liquefaction severity classification is derived with the aim of providing the liquefaction susceptibility maps by defining the LSI (Sonmez and Gokceoglu, 2005).

3. Geostatistical modeling of CPT records

Geostatistical approaches have been applied for many years in geotechnical engineering to assess the spatial variability and the correlation structure in CPT parameters (Jaksa and Fenton, 2000; Liu and Chen, 2010; Wang et al., 2017a). In a typical procedure, the conditional random field is realized through geostatistical simulation to provide the most accurate estimate of CPT records between the measured data over

the entire domain. In this paper, the cross-correlation between the CPT parameters (i.e., tip resistance and side friction) is included as they are highly dependent.

To cover a vast field of application, it is assumed that the mean of the CPT data variations is not a constant value; moreover, the variance increases over an increasingly large region. Therefore, the Sequential Gaussian Simulation (SGS) is exploited along with the ordinary type of Cokriging to generate intrinsically stationary random fields of cross-correlation variables.

In this regard, for each realization, a random path is planned, which crosses all the points at the centroid of elements in the predefined mesh. After characterizing the spatial correlation of random variables by the semivariograms, a search area is defined for each point to identify adjacent known data. In the next step, the mean and variance of the Conditional Cumulative Distribution Function (CCDF) are calculated through the ordinary Cokriging technique. Afterward, one of the CCDF values is picked and added to the initial known data set. This value is assigned to the entire area of the respective element. The procedure is repeated until the random variables for all points are simulated. More details on geostatistical tools, especially the SGS methodology, are addressed in Rouhani et al. (1996), and Webster and Oliver (2007). The geotechnical applications of the SGS can be found in Basarir et al. (2010) and Gholampour and Johari (2019a, 2019b). Details of performing the anisotropic semivariogram analysis are presented in Appendix B.

4. Constructing the sectional random model

In the local or site-scale liquefaction assessment (e.g., near a critical infrastructure or a particular building of interest), the geotechnical exploration programs are usually encountered with limitations and a small amount of measured data is available. Hence, one of the primary challenges in this scale of analysis is constructing a random field model that maximally exploits the limited measured data to improve estimations' accuracy.

In the present study, the random fields of soil properties are determined at sections pivoted around a central axis, perpendicular to the ground surface. Assembling these 2D random fields results in generating a 3D model for soil properties. By using the Sectional Random Field (SRF) instead of the planar field, additional measured data can be involved in the generation of random fields, based on the relatively high sampling frequency of the CPTs in the vertical direction.

In the SRF, the spatial correlation structure is determined in two main steps; in the first step, an anisotropic semivariogram analysis is performed to estimate the initial sections' 2D random field values, by taking the vertical and horizontal correlation into account. The second step is conducting a one-dimensional (1D) rotating semivariogram analysis using angular distances to produce random fields at interior sections. In what follows, the two mentioned steps are described in detail.

4.1. Random field at initial sections

Based on the proposed approach, the final 3D model is considered a cylinder with a specific height and radius, which is involved all locations with CPT sounding (S-1 to S-5 in Fig. 1). As demonstrated in Fig. 1, the circular cross section of the cylindrical model is selected such that the S-1 is the central axis, and the radius, 'R,' is quite large to include other CPT sounding locations. Accordingly, each *initial section* can be appropriately defined such that it contains at least two CPT soundings, where one of them is the central (i.e., sections 1–2 to 1–5 in Fig. 1). Utilizing the maximum number of CPT records at each initial section is the main reason for applying this modeling type. Hence, if the depths of the CPT soundings are different, the bottom of initial section is defined based on the deepest CPT sounding to include all measured data. It is also essential to attentively select a section as an origin (i.e., section 1) and a rotating direction for the analysis (i.e., anticlockwise rotation) to avoid modeling errors.

In the next step, the conditional random fields at the initial sections are generated using the measured data from related CPT soundings. To achieve this aim, the semivariogram analysis is conducted vertically and horizontally. In the vertical direction, the semivariogram model can be accurately fitted based on frequent experimental data points. However, in the horizontal direction, the measured data is so limited that it can only be determined one experimental point for a section with two CPT soundings, which is not sufficient for semivariogram model fitting.

To bypass this problem, two primary assumptions are made; first, the geometry type of anisotropy is considered in the analysis, therefore, the nugget variance (C_0) and the sill (C) are the same in both directions and the anisotropy is only considered for the range parameter at the outset. In the second assumption, for each realization of the initial sections' random field, a value for the degree of anisotropy (ζ) is selected as a random variable to approximate the early value of the horizontal range

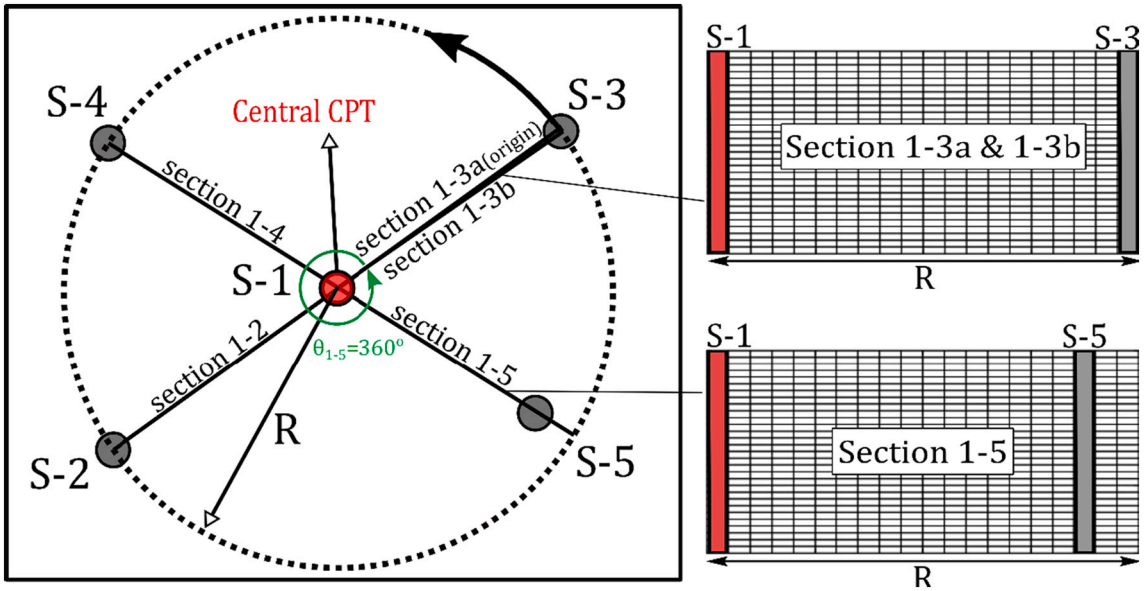

Fig. 1. Details on selecting model geometry and initial sections.

parameter as follows:

$$A_h = \zeta A_v \tag{6}$$

where A_h and A_v are the range parameters in the horizontal and vertical direction, respectively. The mean and standard deviation for ζ is selected based on the study by Cami et al. (2020). In this approach, the initial parameters' values of the horizontal semivariogram models (i.e. A_h, C_0, C) are extracted from a highly accurate vertical model. Then, the parameters' values are finalized based on model fitting, using any existing number of horizontal experimental data (e.g., one data point for initial section with two CPT soundings). More details on this subject are given for the case study in section 7.

After performing the anisotropic semivariogram analysis, the conditional random fields at initial sections are generated through the SGS method, described in section 3. Furthermore, the example of mesh discretization of initial sections is presented in Fig. 1. An additional section (i.e., section 1-3b) is individually considered at the same location with the identical values of the origin section (i.e., section 1-3a) to maintain the model's values' continuity. However, all elements of the last section (i.e., section 1-3b) represents a 360° angle with respect to the origin.

4.2. Random field at interior sections

After generating the conditional random fields at the initial sections, the existing angle between the first and the last initial section (i.e., $\theta_{1-5} = 360°$ in Fig. 1) is divided by '*n*' equal segments. The locations of required sections in the cylindrical model are determined by applying this division. In the present paper, these required random fields are called *interior sections*. They all have the same mesh as the initial sections, and are located around the central axis. It is worth noting that "*n*" represents the number of interior sections.

A particular semivariogram analysis is introduced based on angular distances and the rotational direction to build random fields at interior sections. Performing this analysis results in 1D semivariogram data. It means that the angular distance between pair values at "corresponding elements" of initial sections is utilized in semivariogram analysis. Hence, there will be only one value for the range parameter in the semivariogram model, which is based on angular distances.

In this study, the corresponding elements are defined in which they all have equal coordinates in their sections. The rotating semivariogram model is obtained by considering all sets of corresponding elements. This model merely describes the 1D spatial correlation of random variables in the rotational direction through reasonable computational attempts. Furthermore, the random field values at interior sections are realized through the SGS approach, using the rotating semivariogram model.

As depicted in Fig. 2, each element is spatially identified by its angular distance from the origin section. For instance, the angular distance L_{ij} for E_{ij} (element i in section j) is defined using the following equation:

$$L_{ij} = r_i.\theta_j \tag{7}$$

where θ_j is the angle between section j and the origin section (i.e., section o). r_i represents the horizontal vector distance of element i from the origin line (i.e., central CPT). In this regard, the angular distance, L_{ik} for the element E_{ik} is another example of this identification (see Fig. 2). The separated angular distance between elements E_{ik} and E_{ij} can be readily determined to perform the semivariogram analysis through L_{ik}-L_{ij}. In Fig. 2, the E_{io}, E_{ij}, and E_{ik} are the corresponding elements for vector distance r_i.

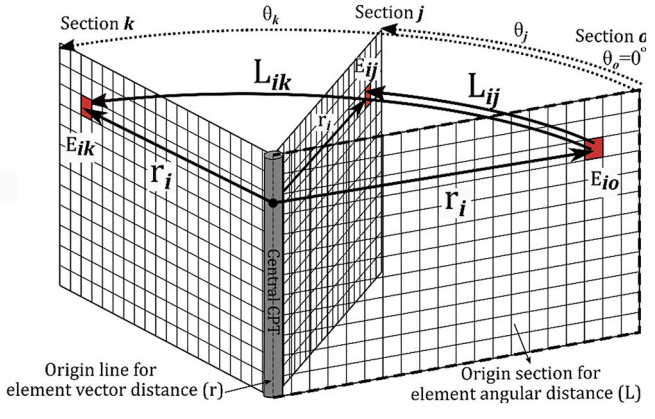

Fig. 2. Rotating semivariogram analysis for corresponding elements based on angular distances.

4.3. The proposed method process

In this section, the practical implementation of the proposed model is described. The steps are schematically presented in detail in Fig. 3 and are as follows:

Step (1) Selecting the central CPT sounding, the cylindrical model radius, and defining the initial sections;

Step (2) Performing 2D anisotropic semivariogram analysis for each initial section, using the measured data from corresponding CPTs;

Step (3) Generating the conditional random fields at initial sections;

Step (4) Performing 1D rotating semivariogram analysis based on all sets of corresponding elements, using the initial sections as the virtual known values;

Step (5) Generating the conditional random fields at interior sections based on a rotating semivariogram model and the virtual known data;

Step (6) Assembling all interior sections data and construct the 3D random field.

Based on the above steps, new conditional random fields for initial sections are generated in each realization of SRF and used as the virtual known data for subsequent random field realization of other interior sections. These steps provide a procedure for generating the SRF for the CPT records. After determining the random fields, the safety factor against liquefaction hazard is calculated by exploiting the described procedure in section 2. These steps are applied to the Monte-Carlo Simulation (MCS) to carry out the probabilistic analysis and determine the spatial distribution of the PL. The generation of SRF is numerously repeated for the probabilistic and spatial assessment of various quantities in liquefaction potential analysis.

The main advantages of the proposed procedure for SRF simulation compared to the mentioned methods in the literature are described in the following:

(a) in the sectional modeling, additional measured data is included in the estimation of random fields, according to the fact that the direction of CPTs is vertical. This modeling strategy causes the soil properties random field to estimate more accurately. Moreover, it is advantageous for examination of the site-scale soil liquefaction problems that are always accompanied by limitations of data measurement;

(b) the spatial correlation of soil properties is particularly modeled in the vertical direction (i.e., parallel to the sedimentation direction which has a relatively smaller scale of variation). The accurate vertical semivariogram model provides an appropriate prediction of the layering characteristics within the soil volume;

(c) the uncertainty in the horizontal correlation of soil properties is included in the semivariogram analysis, by using the degree of anisotropy as a random variable;

(d) apart from the decrease in the computational cost of a random field generation with respect to the LSP approach, the proposed two-step semivariogram analysis (i.e., steps 2 and 4) is remarkably simpler than the generation of 3D semivariogram modeling.

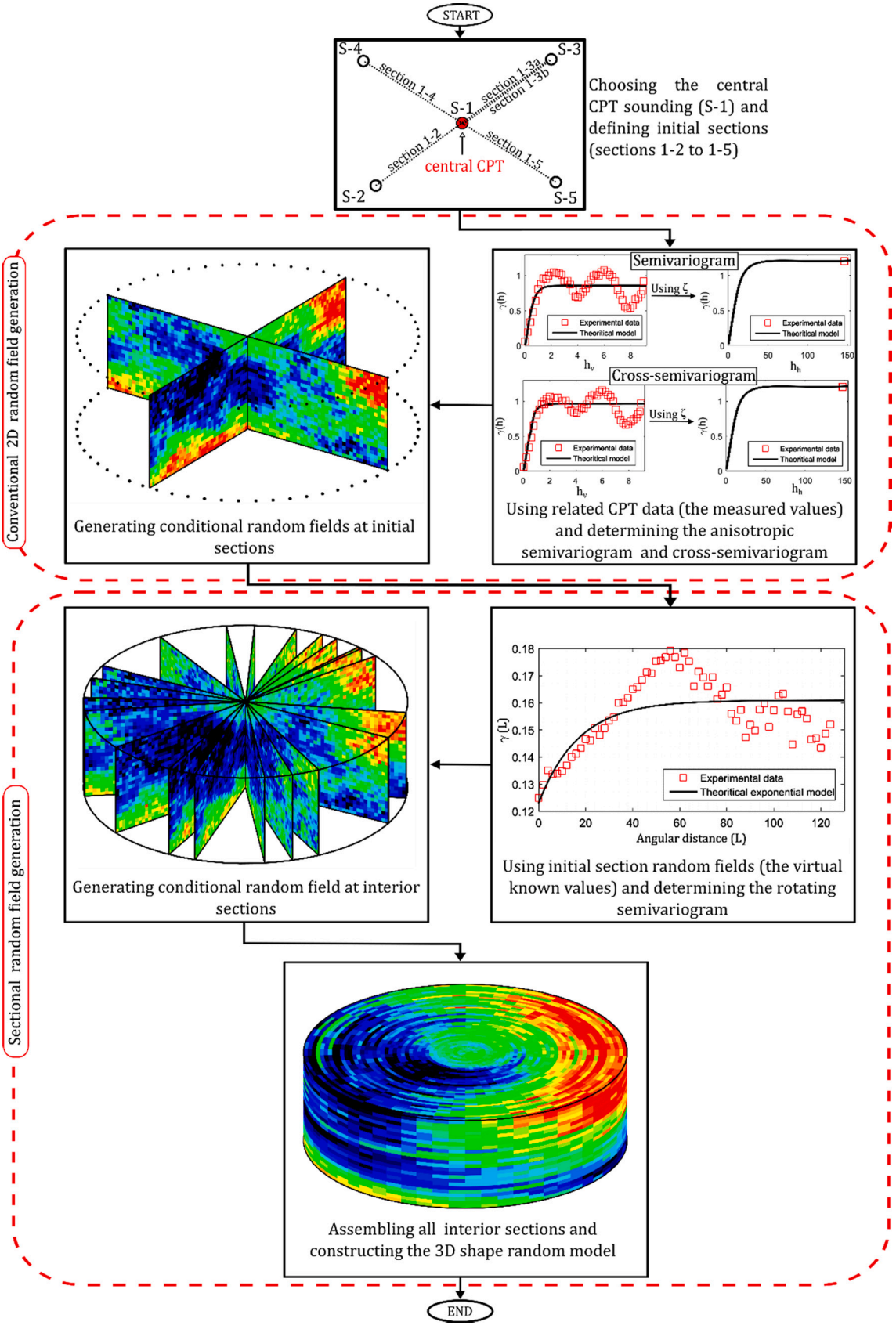

Fig. 3. Flowchart of generating the proposed SRF.

5. Model verification

A procedure for model verification is presented to evaluate SRF realization's performance and assess the efficiency of the coded programs. It must be noted that the primary concern in this section of the paper is to verify the basis and prove the advantages of the model. Details on performing the SRF in a site-scale liquefaction problem are comprehensively described in the next section as a case study.

According to Chen et al. (2017) and Juang et al. (2018), a spatially correlated random field is unconditionally generated for an intended property of soil (e.g., normalized cone resistance, q_{c1N}). In the present study, this random model is called the "*target field*," which is considered a benchmark to validate the SRF realizations. Although a total of 100 sampling points is usually required to reach an acceptable evaluation of the semivariograms in the geotechnical applications (Webster and Oliver, 2007), a virtual field testing plan with 29 CPT soundings is designed here. This number of virtual CPTs is adopted to assess the SRF performance under insufficient measured data which is common in site-scale modeling. There are no limitations in CPT soundings locations, and the field testing points can be in a uniform or radial pattern. To generate the conditional random fields, these synthetic CPT normalized cone resistance values are extracted from the target field at each virtual sounding location. Then, the values are considered as the input known data to implement in the SRF and the LSP approach. The accuracy of the results is assessed by the detailed target field.

As can be observed in Fig. 4 (a), the unconditional random field model is in the form of a rectangular cube by the dimensions of 30 m × 30 m × 8 m, and the corresponding individual mesh size is 1.25 m × 1.25 m × 0.1 m. Therefore, the model is comprised of 46,080 elements. The discretization is selected to find a balance between the accuracy and the reasonable computational effort. It is assumed that normalized cone resistance follows a lognormal distribution. The mean and variance of the parameter are respectively 129.7 and 25, based on the study results of Firouzianbandpey et al. (2015). The spatial structure is specified to be isotropic in the horizontal direction with a 5.0 m correlation length. On the other hand, a spatial variability with 0.45 m correlation length is assumed for the vertical direction (Firouzianbandpey et al., 2015). The uniform layout of virtual testing locations is demonstrated in Fig. 4 (a), specified by white spots. Moreover, the procedure of selecting the initial sections is illustrated to include at least two CPT soundings. In Fig. 4 (a), section 1–1 and locations P_1 to P_4 are marked with black color to be used subsequently for model verification.

A cylindrical model with a 15.0 m radius is selected to construct the SRF realizations. Based on the virtual CPT testing layout, 16 initial sections that are discretized through 1.25 m × 0.1 m elements (i.e., a total of 960 elements) are designed to construct a 2D random field. The element size in the vertical and horizontal direction for sections is identical to that used in the target field. Subsequently, the 3D sectional model is generated by 65 interior sections (i.e., $n = 65$) with a total number of 62,400 elements. In Fig. 4 (b), a typical realization of the proposed model is displayed.

To compare the SRF with the LSP approach, other sets of random fields are generated in a layer-by-layer sequence, where the horizontal correlation is explicitly modeled only. In the LSP approach, random field simulations are performed for each soil layer with a thickness of 0.1 m, using the same planar mesh as the target field. Fig. 4 (c) shows a typical

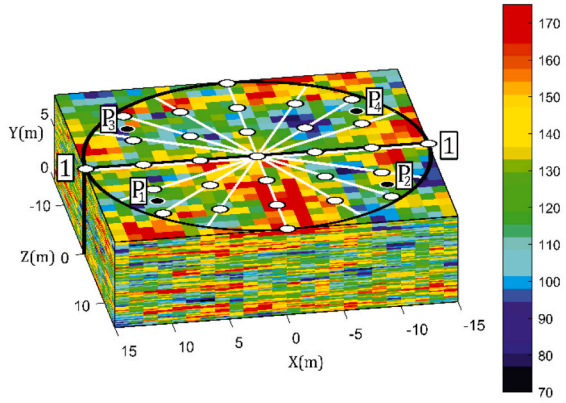

(a) Unconditional random field (target field)

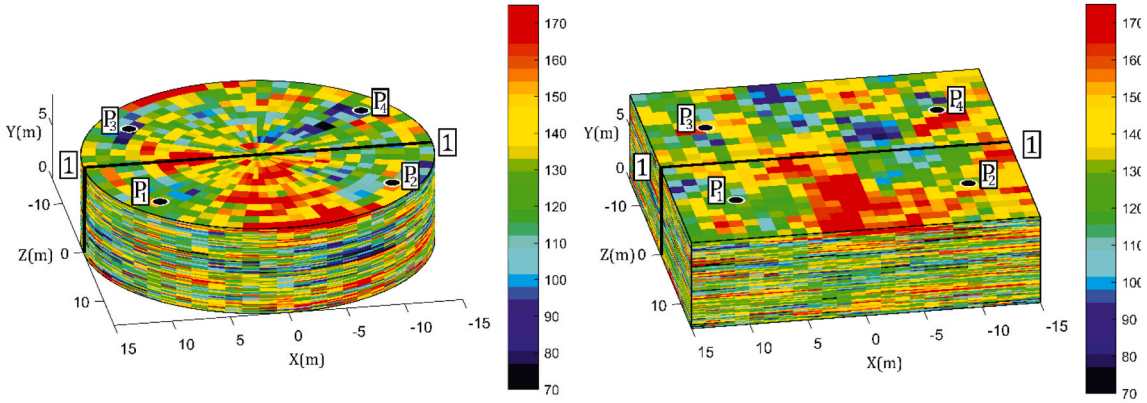

(b) a realization of the proposed SRF (c) a realization of the LSP approach

Fig. 4. Random field for normalized cone resistance.

realization of the LSP approach. In both Fig. 4 (b) and (c), section 1–1 and locations P_1 to P_4 are also marked in order to be used for model verification and comparison.

After constructing a random field realization through both approaches, the computational efficiency of models performance is assessed. Because of the difference in geometric characteristics of the models, it is difficult to provide the exact same circumstances for comparing the SRF and LSP approaches. Nevertheless, the computational time required for calculating the realization of a random field for the SRF and LSP approaches on a personal computer with Intel Core i5–7400 processor and 16 GB memory, are 9 mins and 14 mins, respectively. More computational effort in LSP approach may be related to the 80 times semivariogram analysis, equal to 80 layers, which are required in each realization. Despite the LSP approach, the semivariogram analysis is only performed 17 times, equal to 16 initial sections plus 1 rotational analysis, in the SRF. This difference in computational time cost will be significant for probabilistic analysis where a large scale of random field simulations is needed (e.g., the different time between SRF and LSP reaches 3.47 days for 1000 simulations).

The vertical and horizontal semivariograms for an initial section of the SRF model are demonstrated in Fig. 5 (a) and (b), respectively. In Fig. 5 (a), the model is fitted on sufficient experimental data points which are obtained based on the sectional modeling strategy proposed in this paper. An exponential model with a 0.4 m range parameter is utilized to fit the vertical experimental semivariogram data. The range parameter in the semivariogram model, which is analogous to the correlation length in the SRF, implies that the model can appropriately capture the target field's vertical correlation (i.e., Y-direction). After determining the vertical semivariogram, as mentioned in section 4.1, the horizontal semivariogram is estimated based on initial parameters' values extracted from Fig. 5 (a) and an existing experimental point. Therefore, a 4.1 m range parameter is obtained for the exponential model of horizontal semivariogram.

The vertical and horizontal semivariograms for a layer (i.e., XZ plane) in the LSP approach are shown in Fig. 5 (c) and (d), respectively. As can be seen, the number of measured data points in each layer is equal to the number of soundings locations in the site plan. Since few explorations are usually carried out in site-scale problems, fitting the semivariogram model is specifically difficult in this situation. The absence of sufficient known data may decrease the semivariogram models' efficiency. It is clear from the comparison in Fig. 5, changing the modeling strategy from planar to sectional results in additional measured data usage in the estimation of random fields and consequently, improve the random field's accuracy.

Another method to examine the model prediction ability is by determining the Volume Distribution (VD) of CPT normalized cone resistance throughout the region. This function indicates the occupied volume share of each random variable range in the model. This assessment is provided to check if the random field models can simulate the data distribution of the target field. Fig. 6 demonstrates the VD of a typical SRF and LSP realization, compared with the target field. A cylindrical region corresponding to the SRF of the LSP and target field is considered in the VD evaluation to provide a reasonable comparison. The results indicate that in both approaches, the volumetric distribution of normalized cone resistance is satisfactorily predicted for each range. In the LPI approach, the VD of the target field is predicted within an average of 36% difference. However, the average difference is reduced to 17% for the SRF estimates.

To provide a comprehensive validation and quantitatively assess the model predictive ability, 1000 simulations of q_{c1N} random fields are performed through the SRF and LSP approaches. The expected value of simulations is used at each element in the subsequent analysis. Four locations marked in Fig. 4 (a) to (c) (i.e., P_1, P_2, P_3, and P_4) are implemented to assess the estimated profiles of q_{c1N} which are shown in Fig. 7. For each location, the profile of the target field is plotted and compared with averaged values of SRF and LSP simulations. As can be seen in Fig. 7, the profiles of the LSP approach deviate from the target profile at specific depths (e.g., depth of 3 to 4 m at P_1, P_3, and P_4). These considerable deviations in the LSP profiles indicate information loss and a reduction in the accuracy of prediction ability which can be related to

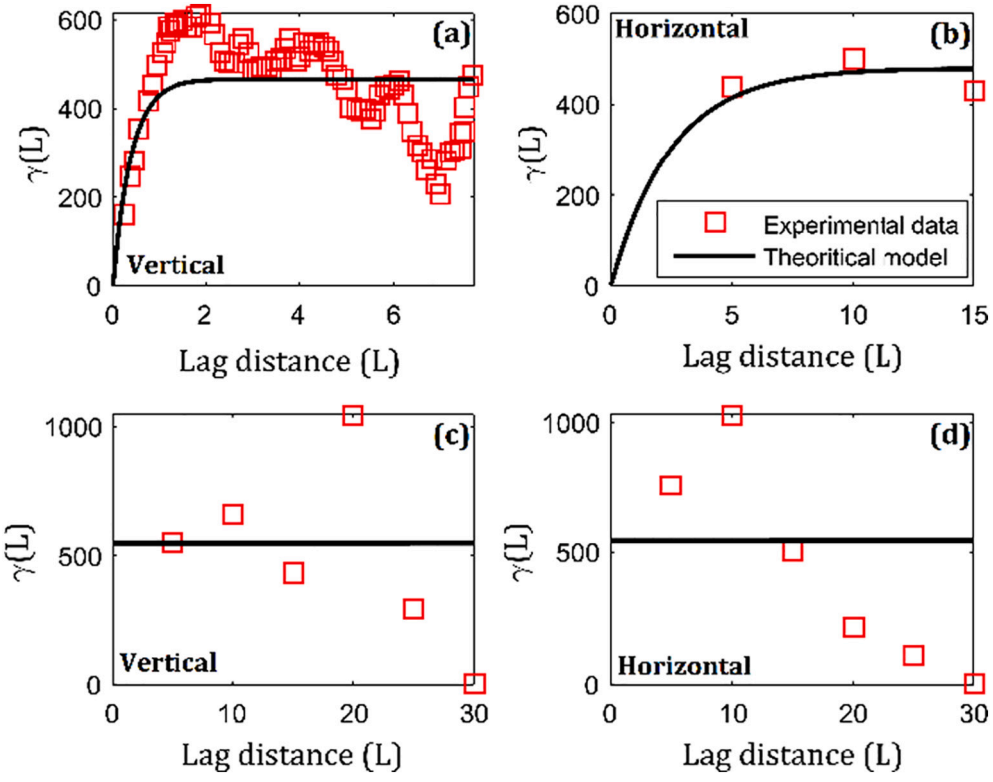

Fig. 5. Semivariogram models for the SRF: (a), (b) and the LSP approach: (c), (d).

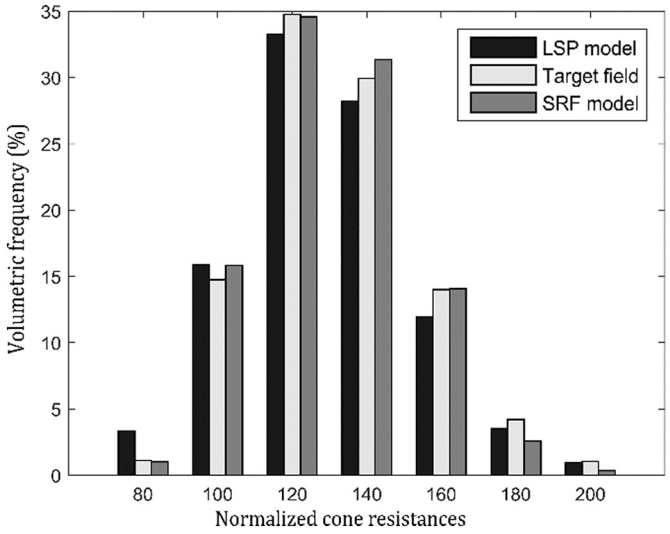

Fig. 6. Comparing the volumetric distribution of normalized cone resistance.

the poor vertical semivariogram model. According to Fig. 7, the SRF approach predicts the q_{c1N} profiles with only less than 10% difference at all four locations, averagely. However, the average difference reaches 24% for LSP predictions.

The target field values versus averaged SRF and LSP simulations are plotted for the section 1–1 and the results are shown in Fig. 8 (a) and (b), respectively. The model predictive validity is quantitatively assessed with the coefficient of determination (R^2), where the more R^2-value closer to one the more accurate model is. As can be seen in Fig. 8, the R^2-value for sampled locations in both SRF and LSP approaches are almost equal to one, which indicates a complete agreement between both estimated values and the target field data. The coefficient of determination for unsampled locations in SRF and LSP are respectively estimated as 0.26 and 0.56. Because of insufficient measured data, both values are relatively small. However, the R^2-value in the SRF is twice bigger than in the LSP approach at unsampled locations which shows better performance of the SRF in site-scale analysis.

6. Liquefaction potential mapping example: Oceano, California case study

A liquefiable site is considered in this section to illustrate the numerical implementation of the SRF in conjunction with the previously described CPT-based empirical model. To conduct a probabilistic analysis, the conditional random fields of CPT records are realized through the suggested approach and implemented as inputs of the empirical model to calculate the liquefaction potential safety factor. The entire process is numerously repeated according to the MCS concept. Thus, a MATLAB-based platform is coded to perform the numerical calculations. This program requires the measured field data, the geometry, and the discretization of the model (i.e., cylinder model dimensions, corresponding initial and interior sections details).

6.1. Site location and geotechnical characteristics

The site is located in Oceano, within the Central Coast Range province of California in the USA. The investigated area is bounded by Cabrillo Highway, Norswing, and Coolidge Drives. Ten CPT soundings are available in this site-scale case study, based on U.S. Geological Survey (2020), and only the first 10 m depth of CPT data is considered for simplicity. In Fig. 9, a satellite overview of the site and the

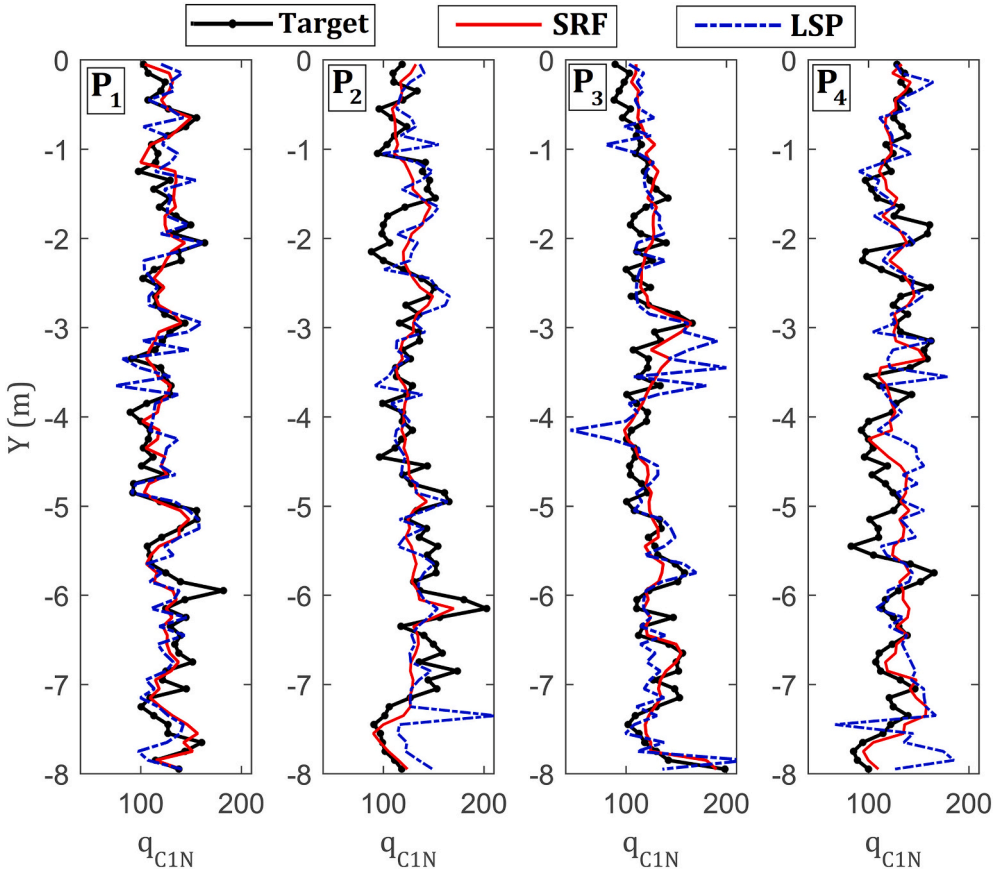

Fig. 7. The q_{c1N} profiles for the target field, SRF and LSP approach at locations P_1 to P_4.

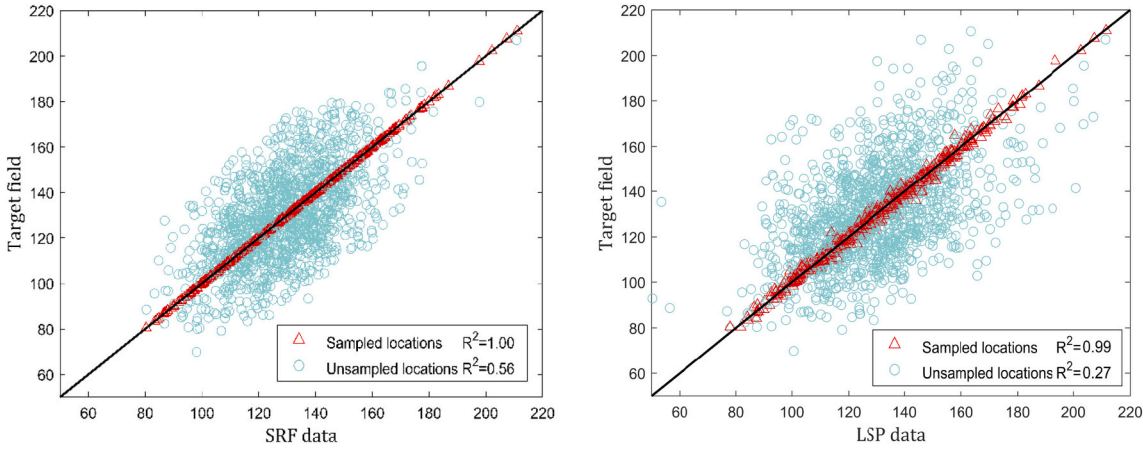

(a) the proposed SRF (b) the LSP approach

Fig. 8. The target field values versus the (a) the porposed SRF and (b) the LSP approach.

approximate CPT soundings locations are jointly demonstrated along with the initial sections. The U.S. Geological Survey (2020) explorations have indicated that the subsurface soil mostly consists of Eolian sand, which is classified as poorly graded sand with silt (SP-SM) and silty sand (SM). Acquired experience of many earthquakes has represented that this sediment type is significantly susceptible to liquefaction in case of being saturated (Youd and Perkins, 1978). Consequently, the located site is in areas with the highest potential of liquefaction and associated lateral spreading in Oceano (Holzer et al., 2005).

In the current paper, the CPT soundings are labeled as S-1 to S-10. As it is common in site-scale projects, the CPT sounding locations are scattered within the studied area. In this analysis, S-1 is selected as the central CPT, and a cylindrical model with 10.0 m height and 84.0 m radius is chosen. In this modeling strategy, there is no limitation on the location of other CPT soundings after the selection of central CPT. For example, S-4, S-5, and S-9 are at a distance of 84.0 m from the center. However, other CPTs (e.g., S-2 or S-10) are closer to the model central axis. This means that the model radius can be arbitrarily selected in order to cover the intended domain. Ten initial sections are selected in the model, and their corresponding numbers are presented in Fig. 9. In this instance, it is assumed that the water table level (d_w) is set at a fixed 0.5 m distance from the ground surface.

At first, the program generates the 2D random fields by the dimensions of 84 m × 10 m, which are discretized by 3.0 m × 0.1 m rectangular elements. Hence, each random model's initial section consists of 2800 elements. Then, 123 interior sections (i.e., $n = 123$) with an equal number of elements are specified. Through this process, a total number of 344,400 elements is exploited for generating the final model. The size and number of elements are attentively selected based on the result accuracy and computing time. Fig. 10 demonstrates the 3D model discretization. In this meshed model, the CPT sounding locations are also specified by red triangles.

In liquefaction potential mapping, it is essential to specify the subsurface conditions. As mentioned by Gong et al. (2020), the uncertainty of a geological model at a given site is categorized in two parts; stratigraphic uncertainty and geo-properties uncertainty. Yet, in this study, the soil characterization is achieved according to CPT results, including the tip resistance and the side friction and only the geo-properties uncertainty is addressed here. In the probabilistic context, these corresponding data and their respective locations are adopted for constructing SRFs in the assessment of spatial variability. The Cokriging method is applied in random field generation, in order to take the cross-correlations between CPT records into consideration.

Since elements with 0.1 m thickness are implemented for discretization, a local averaging is performed to smooth the CPT sounding data at each element. For this purpose, the CPT raw data, which are frequently measured in the vertical direction (taken in 0.05 m intervals), are averaged at 0.1 m intervals, with respect to the utilized element's thickness. Then, the local averages are assigned to the corresponding elements. The CPT data and local averaging for S-10 are indicated in Fig. 11. It is worth noting that the tip resistance is presented in MPa, whereas the side friction is expressed in kPa. The results of local

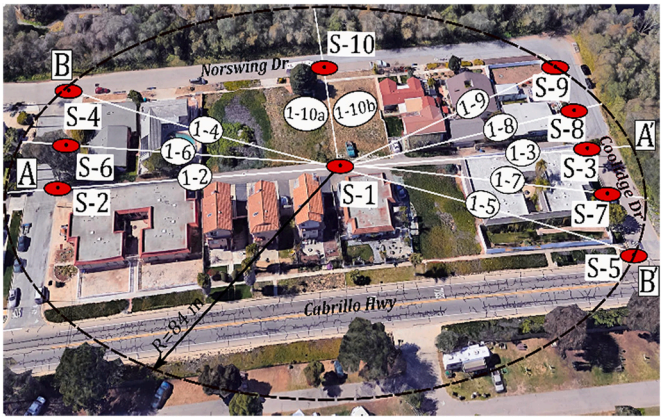

Fig. 9. Satellite overview of the site and the CPT soundings locations.

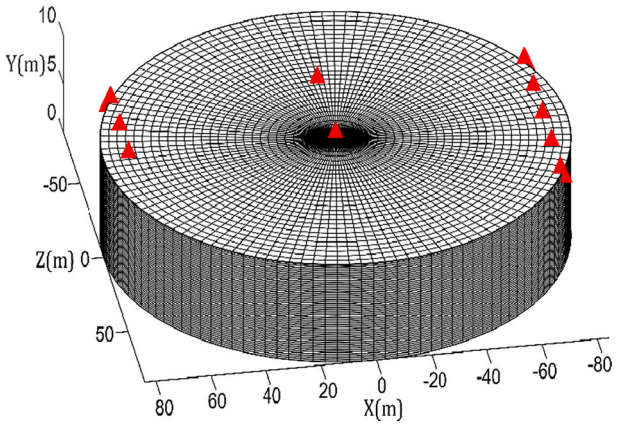

Fig. 10. Discretization process in the proposed random field modeling.

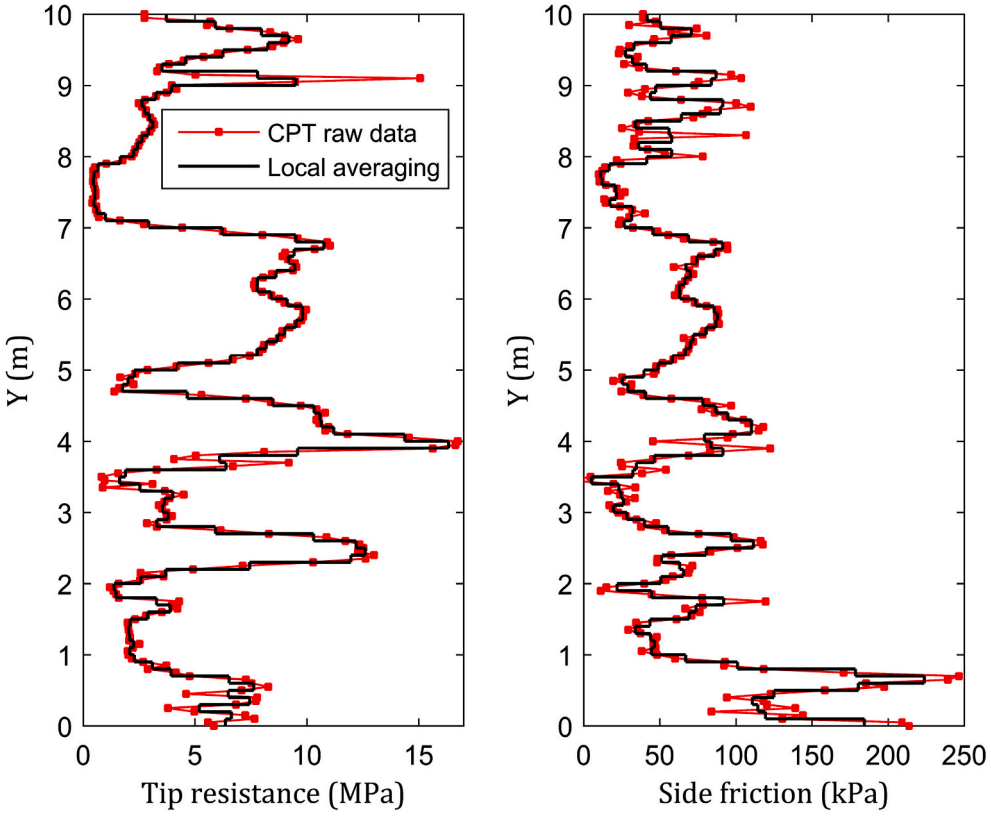

Fig. 11. CPT sounding data and local averaging for S-10.

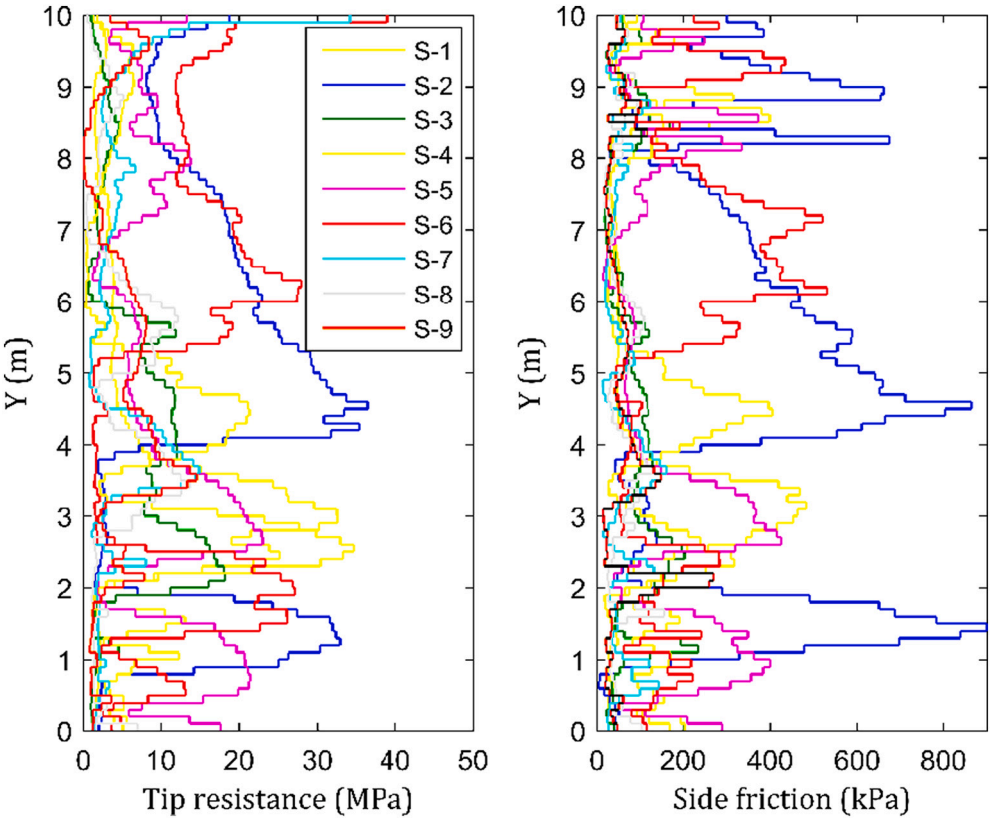

Fig. 12. Results of local averaging for CPT soundings S-1 to S-9.

averaging for other CPT soundings along the depth are illustrated in Fig. 12. The diagrams of Fig. 12 are presented to display the variation domain of measured CPT parameters. This procedure has a negligible impact on the main results. To quantitatively assess this issue, the LPI is calculated at sounding locations, with and without applying the local averaging to the raw CPT data. The outcomes indicate that the mean of differences in the LPI determination results barely reach 2%.

It must be noted that the sole source of uncertainty included in the current probabilistic study is the existing spatial variability of soil properties. Other sources of variability in liquefaction prediction (e.g., earthquake parameters) are not addressed here for simplification purposes. In the liquefaction prediction analysis of the case study, two earthquakes are considered. The first one is the 2003 San Simeon, California, earthquake that caused liquefaction-induced lateral spreading at Oceano. The second one is a hypothetical earthquake based on the characteristics of the Los Osos fault, which is recognized as a high potential fault for creating intense ground shakings (Holzer et al., 2004). The values of the deterministic geotechnical parameters, as well as the parameters of the two corresponding earthquakes, are summarized in Table 1.

7. Results and discussion

7.1. Generation of the SRF

In the first instance, the anisotropic semivariogram analysis is performed for both the tip resistance and the side friction, using the measured data points. Fig. 13 shows the semivariogram models for tip resistance at initial section 1–2 (see Fig. 9). As discussed previously, in the vertical direction, the semivariogram model can be accurately fitted based on frequent experimental data points which are presented by red squares in Fig. 13 (a). Four models (i.e. linear, spherical, exponential, and Gaussian) are examined to obtain the best fitting of semivariograms. For this purpose, two statistical indices (i.e., the residual sums of squares and the coefficient of determination) are provided to assess the models outputs and to investigate how well the models fit the semivariogram data. Based on these indices, an exponential model is chosen and a 0.35 m range parameter is obtained for tip resistance in the vertical direction.

In the next step, a lognormal distribution is assumed for the degree of anisotropy (ξ) which is accounted as a random variable in the proposed approach. The mean and standard deviation of the parameter are respectively adopted as 16 and 4, according to databased reported by Cami et al. (2020). For each realization of the initial section, a random value of ξ is picked and used in the determination of the early value of the horizontal range parameter, based on Eq. (6).

As an example, a theoretical exponential model with a horizontal range of 4.41 m is estimated based on vertical semivariogram range parameter (i.e., $A_v = 0.35$ m) and also a random value of 12.6 for the degree of anisotropy. The final horizontal model is shown by the black line in Fig. 13 (b) which is fitted to the one experimental data point. Because of the random nature of ξ, the horizontal range parameter is a random variable as well where its probability density function is shown in Fig. 13 (b). As can be seen, the A_h is variated between 5.5 m and 30.0 m with the mean value of 14.6 m for this initial section. Other semivariogram models based on the random variability of A_h are also presented in Fig. 13 (b) for 300 simulations. Conclusively, the horizontal range parameters' uncertainty is included in the semivariogram analysis through the proposed approach.

After modeling the semivariogram for CPT parameters, the conditional random fields are generated through SGS across the initial sections. In Fig. 14, the variation of estimated CPT parameters is presented in a typical realization at two sections (i.e., sections *A-A'* and *B-B'* in Fig. 9). Fig. 14 (a) and (b) indicate the random field for tip resistance and side friction at section *A-A'*, respectively. In this regard, section *A-A'* includes the CPT soundings of S-1, S-2, and S-3. Similar to model verification section, the CPT measured values versus the SRF estimates at sampled locations of section *A-A'* are plotted. As expected in conditional random fields, an appropriate agreement (i.e., $R^2 = 0.98$ and $R^2 = 0.99$ respectively for q_c and *f*) is obtained between the estimated values and the measured data at sampling coordinates.

As can be noted, most of the investigated region consists of loose sandy soil, based on a predictive correlation for relative density that has been suggested by Jamiolkowski et al. (2003). However, a very dense sand layer with high CPT parameters' values is recognized in the depth of 5.0 m at the section's left side. This layer is continued to the middle part of the model at a depth of almost 7 m, nearby S-1, and it is almost faded on the right side of the model close by the S-3.

Fig. 14 (c) and (d) represent the random field for tip resistance and side friction at section *B-B'*, respectively. This section involves the CPT soundings of S-1, S-4, and S-5. Once more, a dense sand layer is recognized that is initiated from the left side of the section and is continued to the middle part of the model at a depth of 7 m. Through this layer's proceeding to the section's right side, the layer's depth is enhanced, such that it reaches to around 10 m depth, nearby the S-5. The other parts of the section generally consist of loose sandy soil, which can be considered the prospective zones for liquefaction occurrence.

After constructing random fields at initial sections, they are applied in the 1D rotating semivariogram analysis as the virtual known values. The lag distance is substituted by the angular distance between the corresponding elements to determine the experimental semivariogram data. These data are fitted by exponential model and the results are demonstrated for tip resistance, side friction, and the cross-correlation between them in Fig. 15 (a), (b) and (c), respectively. The corresponding data represents a low variance at close angular distances. While the variance increases by enhancing angular distances and the data express fluctuations.

The random fields at the interior sections are obtained by using these semivariograms, and are merged together to generate 3D random models of CPT parameters. In this regard, Fig. 16 illustrates the final model of a realization for CPT records. Based on the proposed framework's procedure, the model reproduces the initial sections' data at their locations. For instance, the sliced model in Fig. 16 (b) proves that the SRF of tip resistance precisely generates the initial sections 1–2 and 1–5 (Fig. 9), which are located at the left side of section *A-A'* (Fig. 14-a) and the right side of section *B-B'* (Fig. 14-c), respectively. In quantitatively assessing, the values of initial section 1–2 and 1–5 are respectively plotted versus the values at the left and right section of the slice model and consequently the R^2 values of 0.95 and 0.96 are obtained. It is noticeable that the proposed model simulates local fluctuations of CPT records among the initial sections.

The full and sliced SRF model for side friction through one realization are presented in Fig. 16 (c) and (d), respectively. Similarly, it is illustrated that the model regenerates the precise initial section data. As another example, the following point is confirmed in the sliced model presented in Fig. 16 (d) that the exact initial sections 1–2 and 1–5 are generated by SRF for side friction (i.e., $R^2 = 0.97$ and $R^2 = 95$, respectively). These sections are situated at the left side of section *A-A'* (Fig. 14-b) and the right side of section *B-B'* (Fig. 14-d), respectively. After generating the SRF for CPT parameters, the random field for unit weight is constructed using the correlation proposed by Robertson and Cabal (2010). The unit weight for most of the model areas is estimated between 18 and 20 kN/m^3.

By estimating the tip resistance, side friction, and unit weight at each element within the considered model, along with earthquake parameters, the FS against liquefaction occurrence can be acquired through

Table 1
Earthquake and geotechnical parameters required for liquefaction evaluation.

Earthquake	M_w	a_{max} (g)	g (m/s^2)	d_w (m)	γ_w(kN/m^3)
San Simeon	6.5	0.25	9.81	0.50	9.81
Los Osos	6.8	0.40			

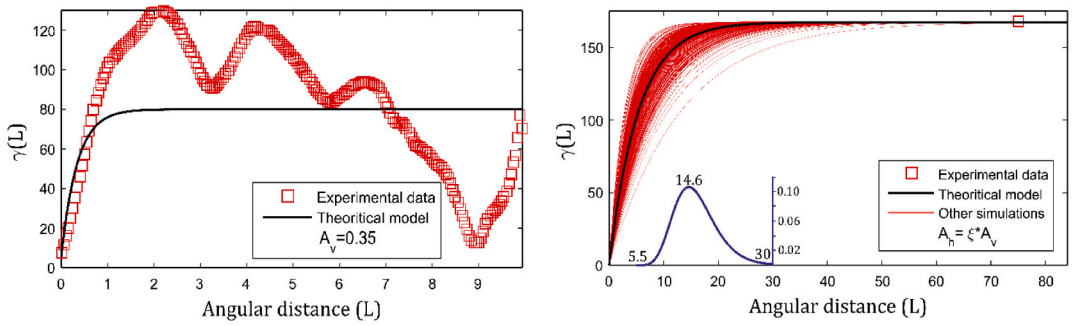

(d) vertical direction (d) horizontal direction

Fig. 13. Semivariogram analysis for an initial section 1–2.

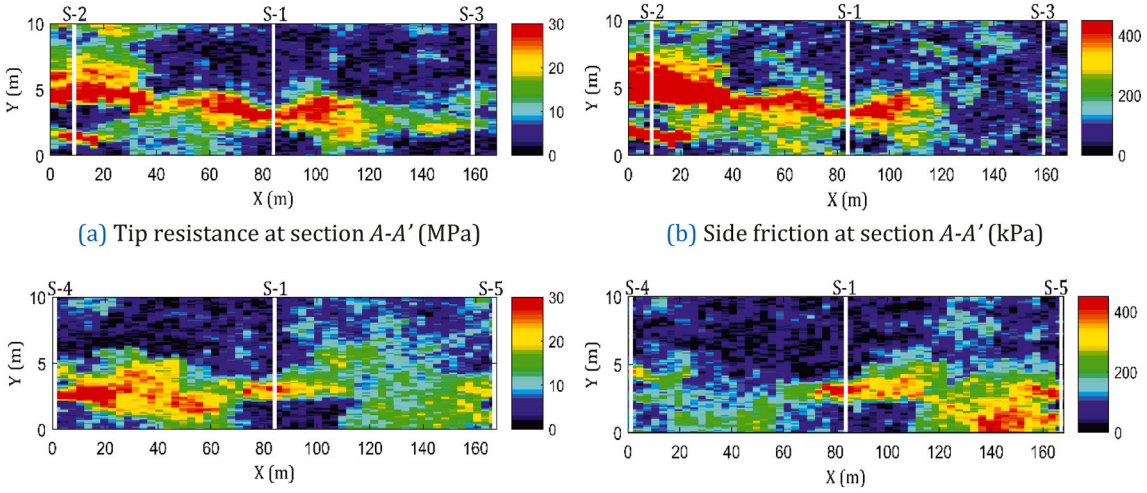

(a) Tip resistance at section *A-A′* (MPa) (b) Side friction at section *A-A′* (kPa)

(c) Tip resistance at section *B-B′* (MPa) (d) Side friction at section *B-B′* (kPa)

Fig. 14. Realization of the 2D conditional random field at two sections.

exploiting the stated method of Section 2. Fig. 17 (a) and (b) present the full and sliced model of FS, respectively, for the Los Osos earthquake parameters (Table 1). Since the FS values are in an extended range, their logarithm is calculated and presented in Fig. 17. In this aspect, the colormap ranges from −1.5 to 1.5 and hence, the areas with negative values correspond to the probable liquefaction occurrence (i.e. FS $\leq$ 1). As expected, the regions valued by high FS correspond with the dense sand layer areas and ground surface.

7.2. *Spatial distribution of the liquefaction probability*

The acquired liquefaction safety factors from the correlation-based approaches are always uncertain to some degree; in other words, it is never entirely precise. Hence, the deterministic methods cannot comprehensively evaluate the liquefaction hazard. To address this problem, the SRF generation steps are replicated in the sense of MCS to assess the liquefaction probabilistic characteristics of the considered site. In this regard, a total of 1000 realizations is performed for both tip resistance and side friction. These random fields are set as inputs to the empirical method described in section 2. Eventually, the process results in 1000 safety factors at each element.

After determining safety factors, the liquefaction probability is acquired by calculating the ratio of the number of FS equal to or less than 1 to the total number of realizations in each element. This parameter evaluates the liquefaction potential throughout the model volume during a specific earthquake. The main concern in the probabilistic analysis is simulating numerous SRF for CPT data to capture the fluctuations between measured points. Other than, determination of the probability can be performed either by classical definition (i.e., as explained above) or Bayesian theory (e.g., formulation by Juang et al., 2003).

As mentioned earlier, two earthquakes are adopted here to analyze the liquefaction potential. The full and sliced model of PL values for the San Simeon, California earthquake are presented in Fig. 18 (a) and (b), respectively. The results indicate that the areas characterized by extremely high PL values are detected at scattered regions of the model. According to Fig. 18 (b), these areas are estimated to be located in the depth of 2 m to 6 m and 8 m to 10 m nearby S-1, and also in the depth of 8 m and 10 m, close by S-2. However, the PL values in surficial regions are almost infinitesimal.

During the San Simeon earthquake, the main cause of destruction to buildings, subsurface facilities and the road surfaces in Oceano has been a lateral spreading due to the liquefaction. The extension zone in lateral

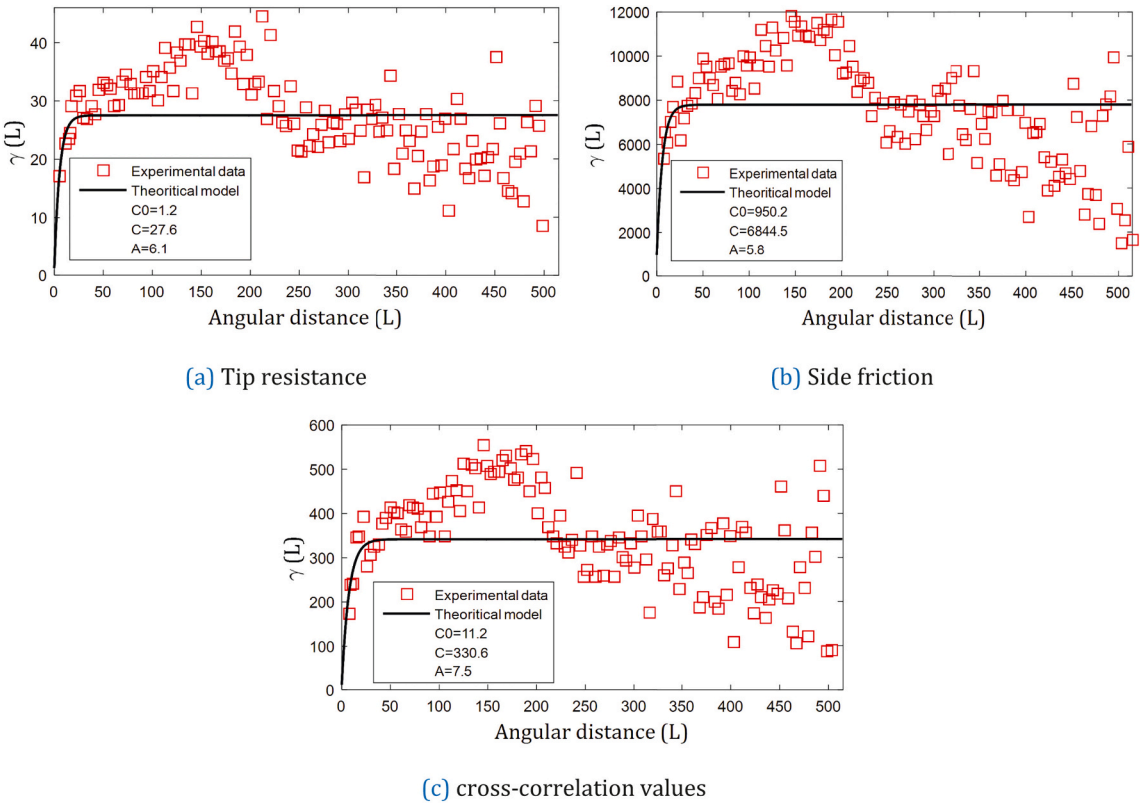

Fig. 15. Rotating semivariogram model.

spreading, where the horizontal translations begin and form the ground cracks, has been started near the S-5. This zone has been obliquely traversed across the central point of the model (i.e., near S-1) and continued to the S-4 location (Holzer et al., 2005). Hence, section *B-B′* in Fig. 9 is selected to assess the predictive ability of the model, based on PL spatial distribution. As can be seen in Fig. 18 (c), the scattered liquefiable zones are jointed together along with this section and create a continuous strip with PL more than 0.55. It can be clearly seen that the projection of the strip on the ground surface is adequately compatible with the observed extension zone.

A sand boiling area has also been noticed in the middle of the considered site which is marked in Fig. 18 (c). Textural properties of sand boils have been indicated that this liquefaction has been primarily localized in an undisturbed Eolian sand area which has been traced at the depth of 4 to 5 m according to the core samples from S-1 (Holzer et al., 2005). As can be seen, a concentrated area with the highest liquefaction probability is evaluated at the depth of 4 to 5 m beneath the marked location which is evidently compatible with the reports.

Fig. 19 (a) and (b) depict the full and the sliced model of PL for the stronger earthquake (the Los Osos), respectively. Using this earthquake's parameters, the scattered areas with high PL are expanded and form continuous stripes along with the model. As presented in Fig. 19 (b), the upper stripe is extended in the depth of 0.5 m to 6 m on the middle and 2 m to 6 m on the model's right side. The lower stripe is expanded in the depth of about 8 m to 10 m throughout the model. This type of information can be advantageous in liquefaction mitigation methods such as ground improvement, in which accurate locating of the liquefiable zone is an essential factor and prevents the implementation of unreliable designs.

7.3. Estimation of liquefaction severity

In the context of estimating liquefaction severity, various quantities (e.g., LPI and LSI) can be defined to assess the seismic hazard. As mentioned before, an acceptable evaluation of liquefaction susceptibility requires detailed calibration of the thresholds based on the observed severity of liquefaction. To calculate the surficial LPI field based on Eq. (3), the averaged safety factors in each element that is arranged in columns at interior sections are jointly utilized with the elements' depth and thickness. In this case study, the reported results of Toprak and Holzer (2003) that are based on LPI thresholds in the California region are considered. These results indicated that liquefaction occurrence initiation is probable where LPI $>$ 5 and its resulting lateral spreads appear where LPI $>$ 12.

Furthermore, the LSI is also evaluated for each column based on PL values to assess the severity of liquefaction and to provide an appropriate platform for comparison of the FS-based and PL-based results. Here, the liquefaction severity classification of LSI proposed by Sonmez and Gokceoglu (2005) is used to map the liquefaction potential of the studied area.

The comparison between LPI and LSI for both earthquakes is demonstrated in Fig. 20. As can be noted in Fig. 20 (a), the model's central region (i.e., around S-1), the right side of the Norswing Drive near the area of the residential buildings (i.e., S-7, S-8 and, S-9), and the left side of Cabrillo Highway show a high degree of susceptibility to liquefaction and lateral spreading (i.e, LPI $>$ 12). Mapping the liquefaction severity for the San Simeon earthquake is also presented in Fig. 20 (b) through LSI. In this regard, the LSI values reach around 0.8 at central areas of the model which is also categorized as high liquefaction severity area. However, the right side of the Norswing Drive and the left side of Cabrillo Highway is laid in the category of moderate liquefaction severity. Therefore, it is realized that the LPI results lead to more conservative estimates of liquefaction severity with respect to the LSI prediction, based on considered classifications.

Fig. 20 (c) and (d) represent the LPI and LSI values for the Los Osos earthquake, respectively. In Fig. 20 (c), it is illustrated that except a small zone in the left, the entire area of the model has LPI $\geq$ 15; thus, they are considered as areas with extremely high liquefaction severity.

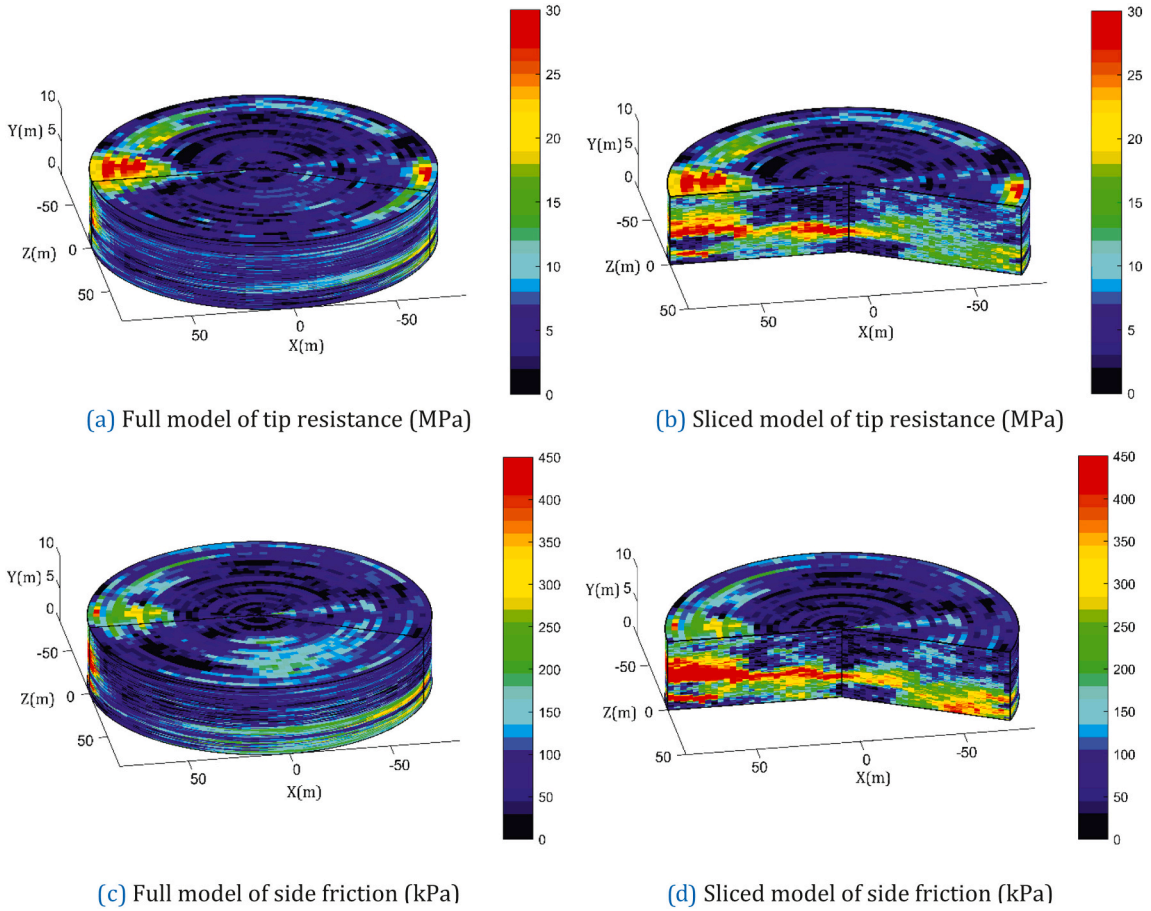

Fig. 16. 3D model of SRF realization.

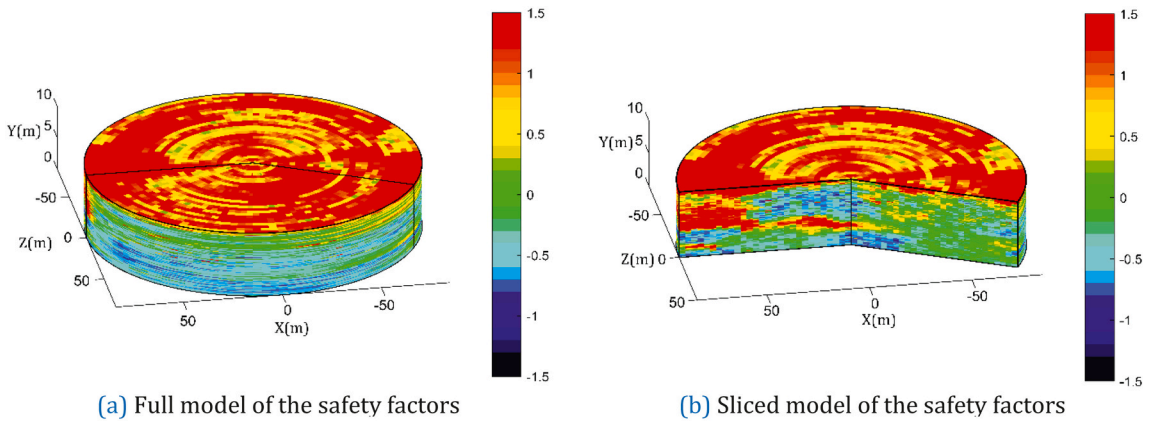

Fig. 17. Estimated safety factors in one realization.

Same results are acquired according to the LSI values in Fig. 20 (d), where the area with high liquefaction probability expands to the central areas of Callibro Highway and also encompasses almost the entire Norswing Drive. However, a more diverse classification for mapping of liquefaction susceptibility is obtained by using the LSI respect to the LPI results.

These results provide advantageous information to predict the surficial liquefaction severity. However, they alone cannot make any predictions regarding the 3D liquefaction-prone zones of the soil depth and its corresponding sections. For example, Fig. 20 illustrate that the least liquefaction potential for both earthquakes is related to the left side of the model, nearby the S-2. While, the PL distribution based on Fig. 18 (b) and 19 (b) express those areas with extremely high liquefaction potential are located in the depth of 8 m and 10 m, precisely under the left side of the model. Consequently, the hazard assessments based on liquefaction severity alone (e.g., the average index approach) cannot provide the comprehensive prediction of liquefaction potential. Since they cannot detect the local liquefiable zone at soil sections, they may lead to unconservative engineering judgments.

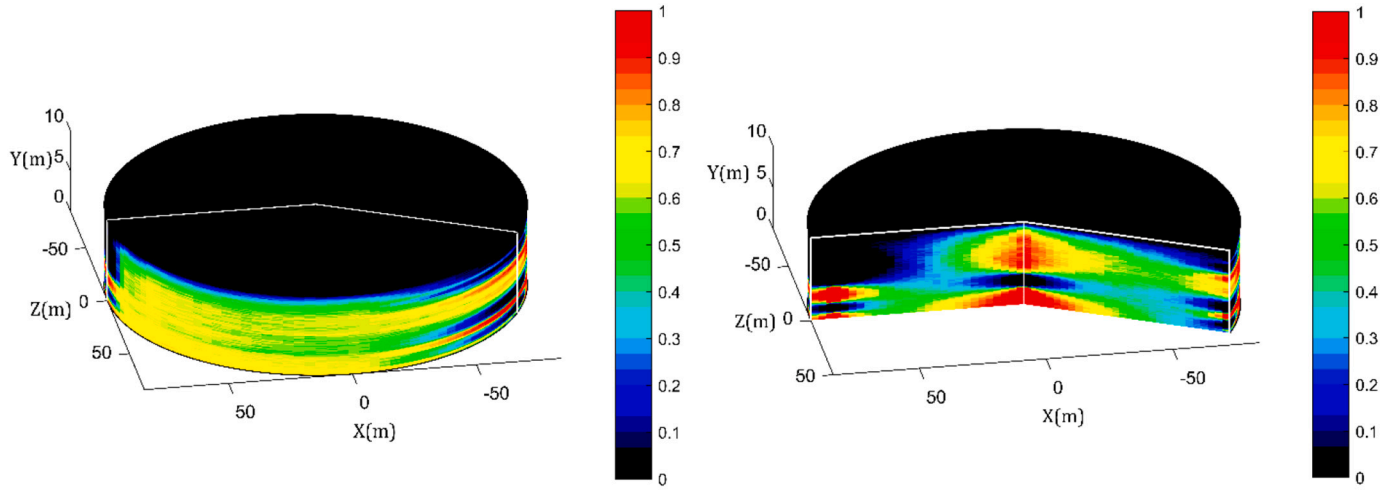

(a) Full model (b) Sliced model

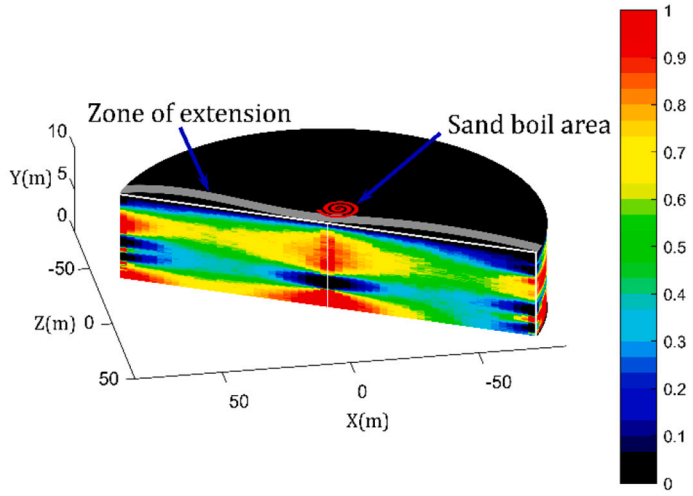

(c) model of section *B-B'*

Fig. 18. The PL Model acquired through 1000 simulations for the San Simeon earthquake.

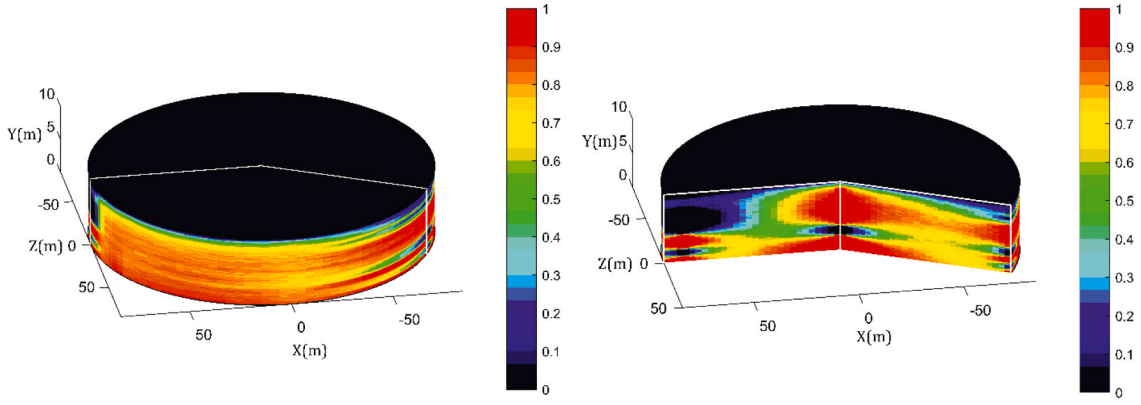

(a) Full model (b) Sliced model

Fig. 19. The PL Model acquired through 1000 simulations for the Los Osos earthquakes.

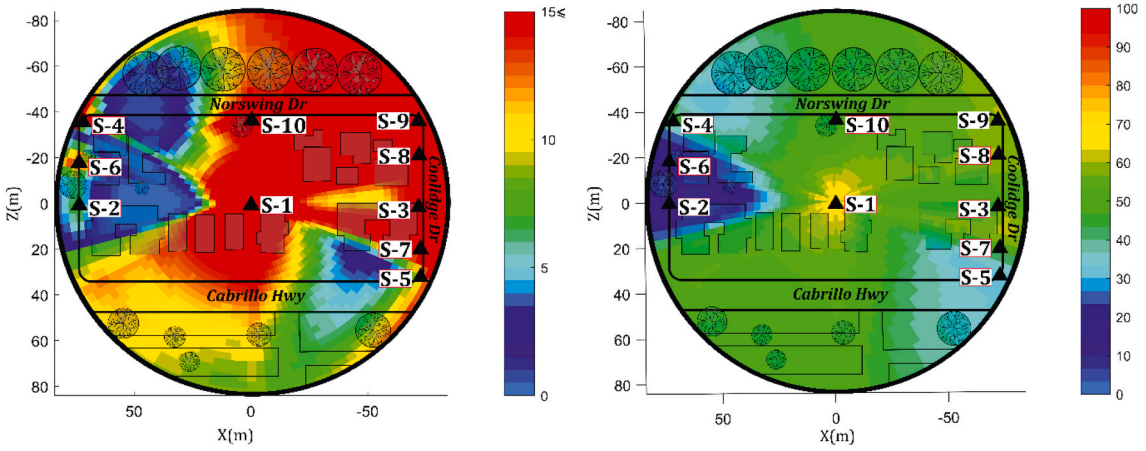

(a) LPI Variation in the San Simeon earthquake (b) LSI variation in the San Simeon earthquake

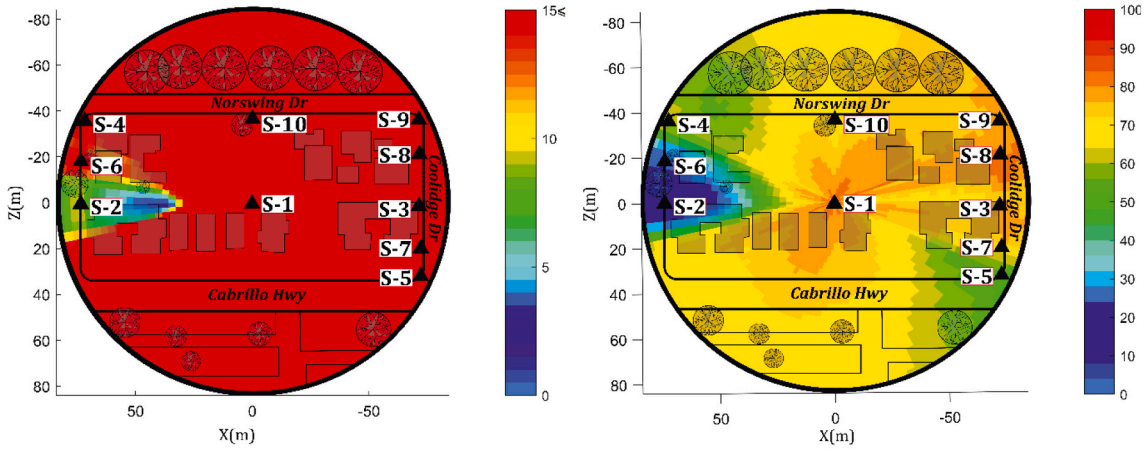

(c) LPI Variation in the Los Osos earthquake (d) LSI variation in the Los Osos earthquake

Fig. 20. Comparison between LPI and LSI at the ground surface in both of the earthquakes.

8. Conclusions

A new modeling technique is proposed to generate a random field in a section-by-section sequence. Since a higher amount of the measured data is included, this strategy increases soil random field estimates' accuracy. Thus, it becomes a beneficial approach for site-scale soil liquefaction problems. Through this method, more accurate vertical semivariogram models are determined which leads to an appropriate estimation of the layering characteristics. Based on the verification procedure, it is demonstrated that changing the modeling strategy from planar to sectional increases the prediction accuracy and reduces the computational effort. The SRF is implemented for a site-scale case study in Oceano, California. According to the evidence in the liquefaction-induced San Simeon earthquake, the proposed approach can efficiently identify the liquefiable zone throughout the soil volume. This type of prediction can be certainly useful in liquefaction mitigation methods such as ground improvement. The liquefaction severity of the case study is also assessed. It is realized that the LPI results lead to more conservative estimates of liquefaction severity with respect to the LSI prediction. However, by using the LSI, a more diverse classification for mapping of liquefaction susceptibility is obtained, especially for strong earthquakes. It is also illustrated that the hazard assessments based on liquefaction severity alone cannot provide the comprehensive prediction of liquefaction potential. Since they cannot detect the local liquefiable zone at soil sections, it may lead to unconservative engineering judgments. In this research, the only included source of uncertainty is the spatial variability of CPT records. Hence, further researches are required to include the uncertainty of earthquake loading into SRF-based probability analysis of liquefaction.

Declaration of Competing Interest

The authors declare that they have no known competing financial interests or personal relationships that could have appeared to influence the work reported in this paper.

Appendix A

The general formulation of the *CSR* is adopted considering the magnitude scaling factor (*MSF*) and shear stress reduction factor (r_d)

$$CSR = 0.65\left(\sigma_v/\sigma_v^{'}\right)(a_{max}/g)(r_d/MSF) \tag{A.1}$$

where σ_v and σ'_v indicate the vertical total and effective stress at the considered depth, respectively. a_{max} is the peak horizontal ground surface acceleration, and g is the acceleration of gravity. Following the study of Youd and Idriss (2001), the magnitude scaling and the shear stress reduction factor are respectively determined by:

$$MSF = (M_w/7.5)^{-2.56} \tag{A.2}$$

$$\begin{array}{ll} r_d = 1.0 - 0.00765z & z \le 9.15m \\ r_d = 1.174 - 0.0267z & 9.15m \le z \le 23m \end{array} \tag{A.3}$$

where M_w represents the moment magnitude of the earthquake, and z indicates the depth of interest. To predict the *CRR*, a CPT-based neural network model, introduced by Juang et al. (2003), is implemented as follows:

$$CRR = C_\sigma exp\left[-2.957 + 1.264(q_{c1N.cs}/100)^{1.25}\right] \tag{A.4}$$

where,

$$C_\sigma = -0.016\left(\sigma_v^{'}/100\right)^3 + 0.178\left(\sigma_v^{'}/100\right)^2 - 0.063\left(\sigma_v^{'}/100\right) + 0.903 \tag{A.5}$$

$$q_{c1N.cs} = \left[2.429I_C^4 - 16.943I_C^3 + 44.551I_C^2 - 51.497I_C + 22.802\right]q_{c1N} \tag{A.6}$$

In Eq. (A.6), q_{c1N} and I_c are respectively defined by:

$$q_{c1N} = \frac{q_c/100}{\sigma_v^{'}/100} \tag{A.7}$$

$$I_C = \left\{(3.47 - log_{10}q_{c1N})^2 + \left[log_{10}\left(\frac{f}{q_c - \sigma_v^{'}}\right) + 1.22\right]^2\right\}^{0.5} \tag{A.8}$$

where q_c and f indicate the measured tip resistance and the side friction, respectively.

Appendix B

The spatial correlation of random functions (i.e., soil properties) is characterized by the semivariogram. The formula for experimental univariate semivariogram $\gamma_{uu}(h)$, is defined as follows

$$\gamma_{uu}(h) = \frac{1}{2N(h)}\sum_{i=1}^{N(h)}[Z_u(x_i) - Z_u(x_i + h)]^2 \tag{B.1}$$

where $Z_u(x)$ and $Z_u(x + h)$ are random functions that evolve with the particular lag vector h. In this formula, $N(h)$ is the number of pairs of data points separated by h. On the other hand, the spatial structure of a pair of cross-correlated variables is described by the cross-semivariogram. The experimental cross-semivariogram for random functions $Z_u(x)$ and $Z_v(x)$ is computed using the following equation:

$$\gamma_{uv}(h) = \frac{1}{2N'(h)}\sum_{i=1}^{N(h)}[Z_u(x_i) - Z_u(x_i + h)][Z_v(x_i) - Z_v(x_i + h)] \tag{B.2}$$

where $N'(h)$ is the number of pairs of data points, separated by 'h', which have measured values of both random function $Z_u(x)$ and $Z_v(x)$. The experimental semivariogram is replaced by a positive definite function, to have a physical meaning. There are several models which are used to fit the experimental semivariogram data (e.g., exponential, Gaussian, and linear function). These models are a function of three parameters; nugget variance, sill, and range. The range parameter, A, is calculated by:

$$A = \sqrt{A_h^2\, cos^2(\alpha - \delta) + A_v^2\, sin^2(\alpha - \delta)} \tag{B.3}$$

where A_h and A_v are the range parameters in the horizontal and vertical direction, respectively. This aspect of the model enables anisotropy determination of soil spatial correlation. In Eq. (B.3), α indicates the angle between pairs, and δ represents the angle of maximum variation, which is set vertically in soils. Further details on the determination of semivariograms can be reviewed in Webster and Oliver (2007).

References

Baker, Jack W., Faber, Michael H., 2008. Liquefaction risk assessment using geostatistics to account for soil spatial variability. J. Geotech. Geoenviron. 134 (1), 14–23.

Ballegooy, Van, Sjoerd, Frederick Wentz, Boulanger, Ross W., 2015. Evaluation of CPT-based liquefaction procedures at regional scale. Soil Dyn. Earthq. Eng. 79, 315–334.

Basarir, Hakan, Kumral, Mustafa, Karpuz, Celal, Tutluoglu, Levent, 2010. Geostatistical modeling of spatial variability of SPT data for a borax stockpile site. Eng. Geol. 114 (3–4), 154–163.

Bong, Taeho, Stuedlein, Armin W., 2018. Effect of cone penetration conditioning on random field model parameters and impact of spatial variability on liquefaction-induced differential settlements. J. Geotech. Geoenviron. 144 (5), 04018018.

Cami, Brigid, Javankhoshdel, Sina, Phoon, Kok-Kwang, Ching, Jianye, 2020. Scale of fluctuation for spatially varying soils: estimation methods and values. ASCE-ASME J. Risk Uncertain. Eng. Syst. Part A: Civil Eng. 6 (4), 03120002.

Caputo, Riccardo, Papathanassiou, G., 2012. Brief communication Ground failure and liquefaction phenomena triggered by the 20 May 2012 Emilia-Romagna (Northern Italy) earthquake: case study of Sant'Agostino-San Carlo-Mirabello zone. Nat. Hazards Earth Syst. Sci. 12 (10), 3177.

Chen, Qiushi, Shen, Mengfen, Wang, Chaofeng, Hsein Juang, C., 2017. Verification of random field-based liquefaction mapping using a synthetic digital soil field. Geotech. Front. 236–245, 2017.

Chung, Jaewon, David Rogers, J., 2017. Deterministic and probabilistic assessment of liquefaction hazards using the liquefaction potential index and liquefaction reduction number. J. Geotech. Geoenviron. 143 (10), 04017073.

Dawson, Kevin M., Baise, Laurie G., 2005. Three-dimensional liquefaction potential analysis using geostatistical interpolation. Soil Dyn. Earthq. Eng. 25 (5), 369–381.

Firouzianbandpey, Sarah, Ibsen, Lars Bo, Griffiths, D.V., Vahdatirad, M.J., Andersen, Lars Vabbersgaard, Sørensen, John Dalsgaard, 2015. Effect of spatial correlation length on the interpretation of normalized CPT data using a kriging approach. J. Geotech. Geoenviron. 141 (12), 04015052.

Geyin, Mertcan, Maurer, Brett W., 2021. Evaluation of a cone penetration test thin-layer correction procedure in the context of global liquefaction model performance. Eng. Geol. 106221.

Gholampour, A., Johari, A., 2019a. Reliability analysis of a vertical cut in unsaturated soil using sequential Gaussian simulation. Sci. Iranica 26 (3), 1214–1231.

Gholampour, A., Johari, A., 2019b. Reliability-based analysis of braced excavation in unsaturated soils considering conditional spatial variability. Comput. Geotech. 115, 103163.

Gong, Wenping, Chao Zhao, C., Juang, Hsein, Tang, Huiming, Wang, Hui, Hu, Xinli, 2020. Stratigraphic uncertainty modelling with random field approach. Comput. Geotech. 125, 103681.

Greenfield, Michael W., Grant, Alex, 2020. Probabilistic regional-scale liquefaction triggering modeling using 3D Gaussian processes. Soil Dyn. Earthq. Eng. 134, 106159.

Holzer, T.L., Noce, T.E., Bennett, M.J., Di Alessandro, C., Boatwright, J., Tinsley, J.C., Sell, R.W., Rosenberg, L.I., 2004. Liquefaction-Induced Lateral Spreading in Oceano, California, during the 2003 San Simeon Earthquake. Open-file Rept 2004-1269. USGS, Menlo Park, CA.

Holzer, Thomas L., Noce, Thomas E., Bennett, Michael J., Tinsley III, John C., Rosenberg, Lewis I., 2005. Liquefaction at Oceano, California, during the 2003 San Simeon earthquake. Bull. Seismol. Soc. Am. 95 (6), 2396–2411.

Iwasaki, T., 1978. A practical method for assessing soil liquefaction potential based on case studies at various sites in Japan. In: Proc. Second Int. Conf. Microzonation Safer Construction Research Application, 2, pp. 885–896, 1978.

Jaksa, Mark B., Fenton, Gordon A., 2000. Random field modeling of CPT data. J. Geotech. Geoenviron. 126 (12), 1212–1216.

Jamiolkowski, Michele, Lo Presti, D.C.F., Manassero, Mario, 2003. Evaluation of relative density and shear strength of sands from CPT and DMT. In: In Soil Behavior and Soft Ground Construction, pp. 201–238.

Juang, C. Hsein, Rosowsky, David V., Tang, Wilson H., 1999. Reliability-based method for assessing liquefaction potential of soils. J. Geotech. Geoenviron. 125 (8), 684–689.

Juang, C. Hsein, Yuan, Haiming, Lee, Der-Her, Lin, Ping-Sien, 2003. Simplified cone penetration test-based method for evaluating liquefaction resistance of soils. J. Geotech. Geoenviron. 129 (1), 66–80.

Juang, C. Hsein, Shen, Mengfen, Wang, Chaofeng, Chen, Qiushi, 2018. Random field-based regional liquefaction hazard mapping—data inference and model verification using a synthetic digital soil field. Bull. Eng. Geol. Environ. 77 (3), 1273–1286.

Kim, Han-Saem, Kim, Mirae, Baise, Laurie G., Kim, Byungmin, 2020. Local and regional evaluation of liquefaction potential index and liquefaction severity number for liquefaction-induced sand boils in pohang, South Korea. Soil Dyn. Earthq. Eng. 106459.

Lee, Der-Her, Chih-Sheng, Ku, Yuan, Haiming, 2004. A study of the liquefaction risk potential at Yuanlin, Taiwan. Eng. Geol. 71 (1–2), 97–117.

Lenz, Jennifer A., Baise, Laurie G., 2007. Spatial variability of liquefaction potential in regional mapping using CPT and SPT data. Soil Dyn. Earthq. Eng. 27 (7), 690–702.

Lin, A., Wotherspoon, L., Bradley, B., Motha, J., 2021. Evaluation and modification of geospatial liquefaction models using land damage observational data from the 2010–2011 Canterbury Earthquake Sequence. Eng. Geol. 287, 106099.

Liu, Chia-Nan, Chen, Chien-Hsun, 2006. Mapping liquefaction potential considering spatial correlations of CPT measurements. J. Geotech. Geoenviron. 132 (9), 1178–1187.

Liu, Chia Nan, Chen, Chien-Hsun, 2010. Spatial correlation structures of CPT data in a liquefaction site. Eng. Geol. 111 (1–4), 43–50.

Na, Ung Jin, Chaudhuri, Samit Ray, Shinozuka, Masanobu, 2009. Effects of spatial variation of soil properties on seismic performance of port structures. Soil Dyn. Earthq. Eng. 29 (3), 537–545.

Özocak, A., Sert, S., May 2010. Evaluation of liquefaction risk by a revised LPI approach. In: 2nd International Symposium on Cone Penetration Testing, Huntington Beach, CA, USA.

Popescu, R., Prevost, Jean-Herve, Deodatis, George, 2005. 3D effects in seismic liquefaction of stochastically variable soil deposits. Geotechnique 55 (1), 21–31.

Robertson, Peter K., Cabal, K.L., 2010. Estimating soil unit weight from CPT. In: In 2nd International Symposium on Cone Penetration Testing, pp. 2–40.

Robertson, P.K., Wride, C.E., 1998. Evaluating cyclic liquefaction potential using the cone penetration test. Can. Geotech. J. 35 (3), 442–459.

Rouhani, Shahrokh, Srivastava, R. Mohan, Desbarats, Alec J., Cromer, Marc V., Johnson, A. Ivan, 1996. Geostatistics for Environmental and Geotechnical Applications, Vol. 1283. ASTM International.

Seed, Harry Bolton, Idriss, Izzat M., 1971. Simplified procedure for evaluating soil liquefaction potential. J. Soil Mech. Found. Div. 97, 1249–1273.

Shen, Mengfen, Hsein Juang, C., Chen, Qiushi, 2019. Mitigation of liquefaction hazard by dynamic compaction—a random field perspective. Can. Geotech. J. 56 (12), 1803–1815.

Sonmez, H., Gokceoglu, C., 2005. A liquefaction severity index suggested for engineering practice. Environ. Geol. 48 (1), 81–91.

Toprak, Selcuk, Holzer, Thomas L., 2003. Liquefaction potential index: field assessment. J. Geotech. Geoenviron. 129 (4), 315–322.

Tunusluoglu, M. Celal, Karaca, Oznur, 2018. Liquefaction severity mapping based on SPT data: a case study in Canakkale city (NW Turkey). Environ. Earth Sci. 77 (12), 1–29.

U.S. Geological Survey, 2020. Earthquake Lists, Maps, and Statistics, accessed December 1, 2020 at URL. https://earthquake.usgs.gov/research/cpt/data/. USGS (2020) Accessed.

Uzielli, M., Vannucchi, G., Phoon, K.K., 2005. Random field characterisation of stress-nomalised cone penetration testing parameters. Geotechnique 55 (1), 3–20.

Vivek, B., Raychowdhury, Prishati, 2014. Probabilistic and spatial liquefaction analysis using CPT data: a case study for Alameda County site. Nat. Hazards 71 (3), 1715–1732.

Wang, C., Chen, Q., 2018. A hybrid geotechnical and geological data-based framework for multiscale regional liquefaction hazard mapping. Géotechnique 68 (7), 614–625.

Wang, Yu, Akeju, Oluwatosin Victor, Zhao, Tengyuan, 2017a. Interpolation of spatially varying but sparsely measured geo-data: a comparative study. Eng. Geol. 231, 200–217.

Wang, Chaofeng, Chen, Qiushi, Shen, Mengfen, Hsein Juang, C., 2017b. On the spatial variability of CPT-based geotechnical parameters for regional liquefaction evaluation. Soil Dyn. Earthq. Eng. 95, 153–166.

Webster, Richard, Oliver, Margaret A., 2007. Geostatistics for Environmental Scientists. John Wiley & Sons.

Youd, T. Leslie, Idriss, Izzat M., 2001. Liquefaction resistance of soils: summary report from the 1996 NCEER and 1998 NCEER/NSF workshops on evaluation of liquefaction resistance of soils. J. Geotech. Geoenviron. 127 (4), 297–313.

Youd, T. Leslie, Perkins, David M., 1978. Mapping liquefaction-induced ground failure potential. J. Soil Mech. Found. Div. 104 (4), 433–446.

Zhang, Yonggang, Xie, Yuanlun, Zhang, Yan, Qiu, Junbo, Sunxin, Wu., 2021. The adoption of deep neural network (DNN) to the prediction of soil liquefaction based on shear wave velocity. Bull. Eng. Geol. Environ. 1–8.

Zhao, Chao, Gong, Wenping, Tianzheng Li, C., Juang, Hsein, Tang, Huiming, Wang, Hui, 2021. Probabilistic characterization of subsurface stratigraphic configuration with modified random field approach. Eng. Geol. 288, 106138.